Acta Pharmaceutica Sinica B 2025;15(7):3545−3560

Chinese Pharmaceutical Association
Institute of Materia Medica, Chinese Academy of Medical Sciences

Acta Pharmaceutica Sinica B

www.elsevier.com/locate/apsb
www.sciencedirect.com

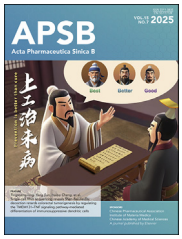

ORIGINAL ARTICLE

Single-cell RNA sequencing reveals Shen-Bai-Jie-Du decoction retards colorectal tumorigenesis by regulating the TMEM131−TNF signaling pathway-mediated differentiation of immunosuppressive dendritic cells

Yuquan Tao[a,†], Yinuo Ma[b,c,†], Limei Gu[d,†], Ye Zhang[a,e], Qinchang Zhang[a], Lisha Zhou[b], Jie Pan[b], Meng Shen[a,f], Xuefei Zhuang[g], Linmei Pan[g], Weixing Shen[a], Chengtao Yu[a], Dan Dong[a], Dong Zhang[a], Tingsheng Ling[d,*], Yang Sun[b,c,*], Haibo Cheng[a,e,*]

[a]*Jiangsu Collaborative Innovation Center of Traditional Chinese Medicine Prevention and Treatment of Tumor, the First Clinical Medical College, Nanjing University of Chinese Medicine, Nanjing 210023, China*
[b]*State Key Laboratory of Pharmaceutical Biotechnology, School of Life Sciences, Nanjing University, Nanjing 210023, China*
[c]*Jiangsu Key Laboratory of New Drug Research and Clinical Pharmacy, Xuzhou Medical University, Xuzhou 221004, China*
[d]*Digestive Endoscopy Center, Affiliated Hospital of Nanjing University of Chinese Medicine, Jiangsu Province Hospital of Chinese Medicine, Nanjing 210029, China*
[e]*Department of Oncology, Affiliated Hospital of Nanjing University of Chinese Medicine, Jiangsu Province Hospital of Chinese Medicine, Nanjing 210029, China*
[f]*Department of Oncology, the First Affiliated Hospital of Soochow University, Suzhou 215100, China*
[g]*Jiangsu Botanical Medicine Refinement Engineering Research Center, Nanjing University of Chinese Medicine, Nanjing 210023, China*

Received 17 January 2025; received in revised form 19 February 2025; accepted 14 April 2025

*Corresponding authors.
E-mail addresses: chinalts@126.com (Tingsheng Ling), yangsun@nju.edu.cn (Yang Sun), haibocheng@njucm.edu.cn (Haibo Cheng).
[†]These authors made equal contributions to this work.
Peer review under the responsibility of Chinese Pharmaceutical Association and Institute of Materia Medica, Chinese Academy of Medical Sciences.

https://doi.org/10.1016/j.apsb.2025.05.013

KEY WORDS

Single-cell RNA sequencing;
Colorectal tumorigenesis;
Tumor microenvironment;
Traditional Chinese medicine;
$CCL22^+$ dendritic cells;
$CD4^+$ regulatory T cells;
TMEM131;
TNF signaling pathway

Abstract Colorectal tumorigenesis generally progresses from adenoma to adenocarcinoma, accompanied by dynamic changes in the tumor microenvironment (TME). A randomized controlled trial has confirmed the efficacy and safety of Shen-Bai-Jie-Du decoction (SBJDD) in preventing colorectal tumorigenesis. However, the mechanism remains unclear. In this study, we employed single-cell RNA sequencing (scRNA-seq) to investigate the dynamic evolution of the TME and validated cell infiltration with multiplex immunohistochemistry and flow cytometry. Bulk RNA sequencing was utilized to assess the underlying mechanisms. Our results constructed the mutually verifiable single-cell transcriptomic atlases in $Apc^{Min/+}$ mice and clinical patients. There was a marked accumulation of $CCL22^+$ dendritic cells (DCs) and an enhanced immunosuppressive action, which SBJDD and berberine reversed. Combined treatment with cholesterol and lipopolysaccharide induced characteristic gene expression of $CCL22^+$ DCs, which may represent "exhausted DCs". Intraperitoneal injection of these DCs after SBJDD treatment eliminated its therapeutic effects. TMEM131 derived $CCL22^+$ DCs generation by TNF signaling pathway and may be a potential target of berberine in retarding colorectal tumorigenesis. These findings emphasize the role of exhausted DCs and the regulatory mechanisms of SBJDD and berberine in colorectal cancer (CRC), suggesting that the multi-component properties of SBJDD may help restore TME homeostasis and offer novel cancer therapy.

1. Introduction

Colorectal cancer (CRC) is one of the leading causes of cancer-related morbidity and mortality worldwide[1]. It develops histologically through a stepwise progression from adenoma to adenocarcinoma, involving intricate biological mechanisms[2]. It is well-established that colorectal tumorigenesis results not only from genetic mutations (such as *Apc* and *Kras*) within tumor cells but also from surrounding cellular crosstalk in the tumor microenvironment (TME)[3,4]. These discoveries raise further questions regarding the main components of the TME, how these constituents transmit signals, and what changes specific components undergo at different stages of CRC progression, resulting in biological effects. It remains unclear whether different subtypes of CRC possess distinct characteristics in their TMEs. More importantly, how can we normalize the TME to prevent and treat CRC?

The TME generally consists of tumor cells, immune cells, stromal cells, vascular cells, and extracellular matrix components. These components interact through cytokines, chemokines, cell surface molecules (such as integrins), adhesion molecules, exosomes, and metabolic products. Novel techniques, including single-cell sequencing, have empowered the exploration of TME[5]. A recent study identified immune suppression mechanisms in early CRC stages and associated genes (such as *DDR1*, *TGFB1*, *PAK4*, or *DPEP1*) with tumor progression[6]. Differences in immune and stromal cells among liver metastases of various CRC subtypes suggest that $SPP1^+$ TAMs have a pro-metastatic function in the TME[7]. For the treatment of CRC, Zhang et al.[8] adopted single-cell sequencing to define myeloid cell lineages and their actions, uncovering the mechanisms of anti-CSF1R and anti-CD40 targeted therapies. Li et al.[9] reported the immune and stromal cellular landscape changes in deficient mismatch repair or microsatellite instability high CRC patients who received toripalimab, a PD-1 inhibitor. Successful immune checkpoint blockade therapy was associated with decreased pro-inflammatory cells and increased anti-tumor immune cells. The application of single-cell sequencing in CRC has led to the identification of intra-tumor heterogeneity and aided in designing personalized treatment based on molecular subtypes and cell populations[10].

The complexity of the TME prevents any single pharmaceutical ingredient from perfectly normalizing all aberrant hallmarks. Traditional Chinese medicine (TCM) is an increasingly acknowledged adjunctive therapy for cancer[11]. TCM focuses on the interaction of drugs and holism, showing its potential in regulating TME[12]. This modulation may lead to progress in therapeutic strategies of TME normalization. Shen-Bai-Jie-Du decoction (SBJDD) is widely used TCM formula consisting of Radix Sophorae Flavescentis, Herba Hedyotis Diffusae, Radix Codonopsis, Rhizoma Atractylodis Macrocephalae, Semen Coicis, Rhizoma Coptidis, Fructus Mume, and Rhizoma Zingiberis Praeparatum. A multicenter randomized controlled trial has demonstrated that SBJDD is effective and safe in preventing recurrent colorectal adenoma[13]. It is noteworthy that the effects and mechanisms of SBJDD on colorectal tumorigenesis and TME are not apparent.

Herein, we hypothesize that SBJDD will regulate colorectal tumor progression *via* altering TME. We will focus on these key objectives: 1) illustrate the TME landscape during colorectal tumorigenesis; 2) explore the mechanism by which SBJDD regulates the TME; and 3) clarify the main components and targets of SBJDD. Here, we established a spontaneous CRC model using $Apc^{Min/+}$ mice and administered SBJDD through oral gavage. Single-cell RNA sequencing (scRNA-seq) was utilized to explore the alterations in cellular composition, differentiation trajectories, and cell crosstalk within the TME during tumorigenesis and SBJDD treatment. Furthermore, we established an immunosuppressive dendritic cells (DCs) model induced by cholesterol and lipopolysaccharide (LPS). We utilized multiplex immunohistochemistry (mIHC) staining, flow cytometry, and bulk RNA sequencing to elucidate the underlying mechanisms. These results reveal the interaction between immune regulation, cholesterol metabolism, and colorectal tumorigenesis and demonstrate a potential strategy for applying TCM to TME modulation.

2. Materials and methods

2.1. Mice and spontaneous CRC model

C57BL/6J mice and B6/JGpt-*Apc*$^{Min/+}$ mice (*Apc*$^{Min/+}$, 4−6 weeks of age) were generated from GemPharmatech Co., Ltd., Nanjing, China, and housed under specific pathogen-free conditions with a 12-h light/dark cycle. *Apc*$^{Min/+}$ mice were fed *ad libitum* with sterile high-fat forage (XTHF60, Jiangsu Xietong Pharmaceutical Bio-engineering Co., Ltd., Nanjing, China) and water. Mice were administered SBJDD *via* gavage (14.1 mg/g). According to the literature, DCs were injected intraperitoneally into mice at 1×10^6 cells per mouse once a week[14,15]. After 12 weeks, the mice were anesthetized with isoflurane gas (1%) and euthanized. Plasmas were collected to assess cytokine levels and total cholesterol content. The colorectum was excised and prepared as "Swiss rolls" to evaluate polyp number, diameter, and histopathology. All animal procedures were performed according to the National Institutes of Health Guide for the care of laboratory animals, with the approval of the Ethics Committee of Nanjing University of Chinese Medicine (202211A031). The key reagents and kits are listed in Supporting Information Table S1.

2.2. Human specimens and tissue microarray

Three colorectal adenoma patients were enrolled and pathologically diagnosed with multiple colorectal adenomas at Jiangsu Province Hospital of Chinese Medicine. Tissue samples were collected for scRNA-seq from patients at initial colonoscopy and after taking SBJDD for 3 months. Tissue microarray samples were pathologically diagnosed at Jiangsu Province Hospital of Chinese Medicine. All patients provided written informed consent. These schemes were approved by the Ethics Committee of the Hospital Affiliated to Nanjing University of Chinese Medicine (No. 2018NL-067-09; 2023NL-003-02).

2.3. Sample preparation

Each colorectal specimen was minced into small pieces (<1 mm) and incubated with 1 mL of collagenase IV and 100 μL DNase in a shaker at 15 °C for about 30 min. After that, 4 mL of Dulbecco's modified Eagle medium was added to dissolve the suspension and filtered through a 70 μm cell strainer. After centrifugation at 250 × *g* for 5 min, the cells were washed twice with phosphate-buffered saline (PBS). The cell pellet was resuspended in 1 mL of ice-cold red blood cell lysis buffer and incubated at 4 °C for 10 min. Then, 10 mL of pre-cooled PBS was added and centrifuged at 250 × *g* for 10 min. After discarding the supernatant, the pellet was resuspended in 50 mL of PBS containing 0.4% BSA. Finally, 10 μL of the suspension was counted under a microscope using trypan blue for cell quantification. After preparing the single-cell suspension, single cells were captured using the 10 × genomics chromium single cell 3′ solution, and sequencing libraries were constructed according to the 10 × genomics sequencing platform's requirements. The raw data have been uploaded to the GEO database (GSE277268).

2.4. Quality control and sample clustering

Using Cell Ranger (v3.1.0) software, 10 × genomics single-cell gene expression data were aligned, barcodes assigned, and unique molecular identifier counts were generated (the reference set GRCh38−3.0.0). The filtered count matrix was converted into a sparse matrix using the Seurat package[16] (v4.3.0) in R. Cells expressing fewer than 200 genes or more than 40,000 genes, and cells with mitochondrial reads exceeding 20% were excluded from further analysis. After filtering, the data were log-normalized and scaled to adjust for cell-to-cell variation due to differences in unique molecular identifier counts and percentage of mitochondrial reads. The single-cell data were integrated and corrected using the Harmony package to mitigate batch effects. Then, cells were clustered using the "Find Clusters" function (resolution = 0.8), and their identities were defined using the top ten principal components generated from PCA analysis. The "RunUMAP" function was used for dimensionality reduction and visualization. We extracted different cell types for sub-group clustering and clustered them at multiple resolutions based on the visual inspection using their respective top 20 PCs.

2.5. Inference of the copy number variation (CNV) in malignant tumor cells

The InferCNV software package (version 1.14.2) was used to infer the CNV in EPCAM$^+$ epithelial cells. Myeloid cells were used as a reference. The CNV signal for each cell was estimated using a 100-gene-wide sliding window. Genes with an average count of less than 0.1 across all cells were filtered out before analysis, and the signals were denoised using a dynamic threshold set at 1.3 times the standard deviation relative to the mean. For each sample, the CNV score was calculated using the sum of squares of each gene expression minus one and was corrected based on the expression levels of the reference cells, resulting in the final CNV score.

2.6. Gene enrichment analysis

To identify differentially expressed genes (DEGs) between groups, the Find Markers function of the Seurat package, which employs the Wilcoxon rank-sum test algorithm, was used with the following criteria: (1) logFC >0.25; (2) $P < 0.05$; (3) pct >0.1. Based on the identified gene sets displaying differential expression, Gene Ontology (GO) enrichment analysis was conducted separately for upregulated (logFC >1) and downregulated genes (logFC < −1) using the Cluster Profiler package[17].

2.7. Cell abundance scoring

The DEGs (logFC >2) of each cluster were provided as input to the AUCell R package[18] (version 1.20.2). The cancer genome atlas (TCGA) COAD bulk RNA sequencing dataset was used as the input for Area Under the Curve (AUC) calculations. The AUC values were used to establish a gene expression ranking for each cell, which was then used to determine the proportion of highly expressed genes in TCGA samples from the differential gene sets of each cell. This method was used to calculate cell abundance in each sample.

2.8. Pseudo-time analysis

The Monocle 2 R package (version 2.24.0) was used for pseudo-time analysis[19]. Its input genes were the top 30 markers for each myeloid cell subpopulation. These analyses were performed using the functions newCellDataSet, estimateSizeFactors, and estimateDispersions. The detectGenes function filtered out low-quality cells with "min expr = 0.1".

2.9. Cellular interaction analysis

CellChat[20], a public database tool based on ligands and receptors, was used to examine cell−cell communications. CellChat uses gene expression data given by the users to estimate the probability of cell−cell communication through an existing database and a model based on gene expression. It allows for the computation of the interaction, which means the significance of cell communication, thereby determining the probability and strength of ligand−receptor interactions between 2 clusters.

2.10. Cell isolation and culture

Bone marrow cells and induced Tregs were prepared under standard protocols described previously[21-23]. Cells were cultured in lymphocyte culture medium (RPMI 1640 medium supplemented with 10% fetal bovine serum, 100 units/mL penicillin, 100 μg/mL streptomycin, 50 μmol/L 2-mercaptoethanol, and 10 mmol/L HEPES). Bone marrow cells were cultured with 20 ng/mL recombinant mouse GM-CSF and 5 ng/mL IL-4. Suspended cells were collected and plated after 8 days in culture. To induce Tregs, spleen single-cell suspensions were prepared, and red blood cells were lysed before the isolation of $CD4^+CD62L^+$ T naïve cells using magnetic bead sorting. Cells were then seeded in 12- or 24-well plates pre-coated with anti-CD3ε antibody (4 μg/mL) and supplemented with IL-2 (20 ng/mL), TGF-β (5 ng/mL), and anti-CD28 antibody (2 μg/mL) stimulation for 5 days to induce Treg differentiation. The key antibodies and recombinant proteins used in this study are listed in Supporting Information Table S2.

2.11. RT-PCR and quantitative PCR (qPCR)

Total RNA was extracted from cells or tissues using TRIzol reagent (Invitrogen, Carlsbad, CA, USA, Cat# 15596018CN). The concentration and purity of RNA were determined using NanoDrop 2000 Spectrophotometers (ThermoFisher, Waltham, MA, USA, ND2000). Complementary DNA (cDNA) was synthesized using HiScript II Q RT Super Mix (Vazyme, Nanjing, China, R223-01) on a Veriti 96-Well Fast Thermal Cycler (ThermoFisher, 4375305). The mRNA expression was quantified using ChamQ Blue Universal SYBR qPCR Master Mix (Vazyme, Q312-02). qPCR was performed on QuantStudio 5 Real-Time PCR System (ThermoFisher, A28574). The primer sequences used for qPCR are listed in Supporting Information Table S3. Gene expression levels were quantified using the $2^{-\Delta\Delta Ct}$ method with β-actin as the normalization control.

2.12. Cell infection

Three short hairpin RNAs (shRNAs) targeting TMEM131 and negative control plasmids (plV3ltr-ZsGreen-Puro-U6) were obtained from Nanjing Corues Biotechnology Co., Ltd. (Nanjing, China). The oligo sequences of TMEM131 shRNAs are listed in Table S3. $CCL22^+$ DCs were infected with lentivirus supernatant (MOI = 100). The efficiency of Tmem131 knockdown was detected by RT-PCR 72 h after infection.

2.13. Flow cytometry

Cells were harvested and washed with Dulbecco's phosphate-buffered saline (Basal Media, Shanghai, China, B210KJ) and then incubated with Fixable viability stain 780 (BD Biosciences, San Jose, CA, USA, 565388) for 10 min. Subsequently, cells were washed with PBS containing 2% FBS and harvested with purified anti-mouse CD16/CD32 (BD Biosciences, 553141) to block nonspecific binding. For cell-surface protein staining, cells were incubated with cocktails of antibodies for 25 min at 4 °C. Cells were fixed and permeabilized for nuclear protein staining using the Foxp3/transcription factor staining buffer set (eBioscience, San Diego, CA, USA, 00-5523-00). Following staining, cells were resuspended in PBS and analyzed using a flow cytometer (Beckman Coulter, Brea, CA, USA, Cytoflex). FlowJo software (V10) was used for data analysis. A gating strategy was established based on forward scatter (FSC) and side scatter (SSC) properties to exclude dead cells and doublets. Data are represented as the percentage of positive cells within the gated population or MFI values.

2.14. Hematoxylin and eosin staining and immunohistochemistry (IHC) staining

Sections were sequentially deparaffinized with xylene and rehydrated in a descending ethanol series. Hematoxylin was applied for nuclear staining, followed by rinsing under tap water. Eosin was used for cytoplasmic staining. Subsequently, the slides were dehydrated in an ascending alcohol series, cleared in xylene, and covered with a cover slip. Histological examination was conducted using a light microscope.

For IHC, the slides' deparaffinization and rehydration processes were the same as above. Antigen retrieval was carried out using citrate buffer (pH 6.0). They were then cooled to room temperature, and endogenous peroxidase was blocked by 3% hydrogen peroxide for 20 min. Nonspecific binding was blocked by incubating sections with 5% goat serum in PBS for 1 h at room temperature. The primary antibodies were diluted to an appropriate concentration according to the manufacturer's instructions and applied to each section, followed by overnight incubation at 4 °C in a humidity chamber. After primary antibody incubation, sections were washed in PBS and incubated with a horseradish peroxidase-labeled secondary antibody at room temperature for 1 h. The target antigen sites were visualized with 3,3′-diaminobenzidine as the chromogen, providing brown coloration. Finally, IHC sections were counterstained with hematoxylin, dehydrated in an ascending series of ethanol followed by xylene for 20 min, and mounted beneath a cover slip. Slides were examined under a light microscope, and images were captured for further analysis. The staining intensity was quantified using ImageJ software.

2.15. mIHC staining

The sections were pretreated as in IHC. Following the manufacturer's instructions, sections were incubated with 5% goat serum, primary antibody, and secondary antibody at room temperature for 30 min each, and signal amplification dye at room temperature for 10 min. After each cycle, antigen retrieval was performed, establishing a repeated cycle for each additional antibody staining. After incubation, sections were washed in PBS to remove unbound antibodies and then counterstained with DAPI (4′,6-diamidino-2-phenylindole) for nuclear visualization. Finally, sections were mounted using an anti-fade mounting medium to prevent fluorescence quenching. Images were captured using a laser confocal microscope, and quantitative analysis was performed using Halo v3.0.311.314 software.

2.16. ELISA

Following the manufacturer's instructions, samples and standards were prepared and then added to wells of microtiter plate pre-coated with a primary antibody specific for the target protein. The microplate was incubated at 37 °C for 1 h and then washed to remove unbound components. After washing, 50 μL of substrate A and substrate B were each added to all the plate wells and then incubated in the dark at 37 °C for 15 min. The reaction was stopped with a stop solution, followed by measuring optical density values at 450 nm in a microplate reader.

2.17. Statistical analysis

Statistical analysis was conducted using IBM SPSS Statistics 26. Values are presented as mean ± standard deviation (SD). Group differences were assessed using Student's *t*-test or one-way ANOVA, with a significance level set at $P < 0.05$. Post-hoc tests were conducted for multiple comparisons. The Mann−Whitney U test was used to analyze non-parametric data. Correlations were evaluated using Pearson's correlation. For single-cell sequencing data, differential expression analysis was performed using the Wilcoxon rank-sum test. Data visualization was performed using GraphPad Prism 9 and R 4.2.2.

3. Results

3.1. SBJDD inhibited colorectal tumorigenesis

High-fat diets have been shown to promote colorectal tumorigenesis[24]. To investigate the effect of SBJDD on this process, we established a spontaneous colorectal tumorigenesis model and administered SBJDD twice daily (Fig. 1A, Created in BioRender, agreement number: RG27ZPMIFY). From the sixth week, the body weight of mice in the $Apc^{Min/+}$ group was significantly higher than that of the normal group. However, there was no noticeable increase in body weight in the mice treated with SBJDD (Supporting Information Fig. S1A). Further analysis suggested that the weight gain in the $Apc^{Min/+}$ group was primarily due to increased abdominal fat (Fig. S1B). SBJDD significantly reduced the number and volume of colorectal tumors (Fig. 1B−D). Regarding pathological grading, SBJDD reduced the malignancy grade of colorectal tumors (Fig. 1E). SBJDD also remarkably decreased the percentage of Ki67-positive cells in tissues (Fig. 1F and G).

3.2. Changes in the single-cell transcriptomic atlas

scRNA-seq (10 × Genomics) was performed to clarify the changes in TME during tumorigenesis and SBJDD treatment. After numerous quality control steps, 48,992 cells were generated for single-cell transcriptome analysis. Five major cell types (including epithelial cells, stromal cells, myeloid cells, B cells, and T cells) were defined by clustering the expression levels of characteristic molecules after preprocessing and dimensionality reduction (Fig. 1H). Subsequently, each compartment was further preprocessed, dimensionality reduced, clustered, and annotated, identifying 40 distinct cell subtypes (Fig. 1I).

3.3. Highly heterogeneous CNV patterns in epithelial cell types

To further define the malignant state of epithelial cells, we used myeloid cells as the reference to infer single-cell CNV profiles of epithelial cells. Epithelial cells were annotated and divided into seven subgroups, including goblet cells, stem cells, and $Saa1^+$ enterocytes (Fig. S1C). Gene mutations on different chromosomes are shown in Fig. S1D. As expected, the frequency of gene mutations in the SBJDD group was lower than in the $Apc^{Min/+}$ group. Based on the results of the CNV analyses, we conducted CNV scoring for epithelial cells and their subgroups to assist in identifying malignant tumor cells. The results indicated that the CNV scores in the $Apc^{Min/+}$ group were significantly higher than those in the SBJDD group (Fig. 1J), particularly in the four cell subgroups: goblet cells, stem cells, tuft cells, and TA cells (Fig. 1K, Fig. S1E).

3.4. Dynamic alterations of $CCL22^+$ DCs in the TME

To further characterize the variation of TME among groups, we annotated the cell types of each group separately. The results indicated that the $Apc^{Min/+}$ group has higher myeloid cell and T cell composition ratios than normal or SBJDD-treated groups. In contrast, it shows lower stromal and B cell percentages than normal or SBJDD-treated samples (Supporting Information Fig. S2A). Differential composition ratios of various cell subgroups were also detected (Fig. S2B). Besides, we analyzed the ratio of observed to expected cell numbers (Ro/e), which indicates how enriched each of these subclusters was to a particular tissue. The Ro/e values exceeded 1 and were considered clusters significantly enriched in the tissue[25]. We found that $Nlrp3^+$ TAMs, neutrophils, stem cells, $Ccl22^+$ DCs, $Spp1^+$ macrophages, $Cd4^+$ regulatory T cells (Tregs), and $Cd4^+$ Th17 cells were significantly enriched in the $Apc^{Min/+}$ group. These subgroups' enrichment scores significantly decreased after treatment with SBJDD (Fig. 2A).

Furthermore, we evaluated the activity of these gene sets in each cell by computing AUCell scores for given cell subgroups with TCGA database. Strikingly, most cell clusters, including $NLRP3^+$ TAMs, neutrophils, $CCL22^+$ DCs, $SPP1^+$ macrophages, $CD4^+$ Tregs, and $CD4^+$ Th17 cells, showed significant differences between CRC and normal tissue, especially for the $CCL22^+$ DCs (Fig. 2B). We also defined the potential marker genes of the $Ccl22^+$ DCs with high expression of *Ccl22*, *Ccl17*, *Ccr7*, and *Fscn1* and low expression of *Mptx1*, *Agr2*, and *Dcn* (Fig. S2C and S2D). mIHC results demonstrated a significant increase in the infiltration of $CCL22^+$ DCs in the $Apc^{Min/+}$ group, significantly decreasing after SBJDD treatment (Fig. 2C and D). qPCR revealed that *Ccl22* and *Ccl17* mRNA were significantly elevated in the $Apc^{Min/+}$ group but significantly reduced after SBJDD treatment (Fig. S2E). We also measured the CCL22 and CCL17 levels in the plasma of mice from different groups. Plasma CCL22 and CCL17 levels were significantly higher in the $Apc^{Min/+}$ group than in the normal group, but no further decrease was observed after the SBJDD treatment (Fig. S2F).

3.5. Development trajectory and evolutionary dynamics of myeloid cell subtypes

It is worth noting that $Ccl22^+$ DCs are possibly involved in colorectal tumorigenesis because they were dramatically induced in the $Apc^{Min/+}$ group. $Ccl22^+$ DCs were identified as a subtype of myeloid cells, which were further classified into 9 distinct types: Mono/Macrophages, $Ly6c2^+$ Monocytes, and $Wdfy4^+$ DCs (Fig. 2E). Supporting Information Fig. S3A shows the characteristic marker genes of these myeloid cells. We used a monocle to

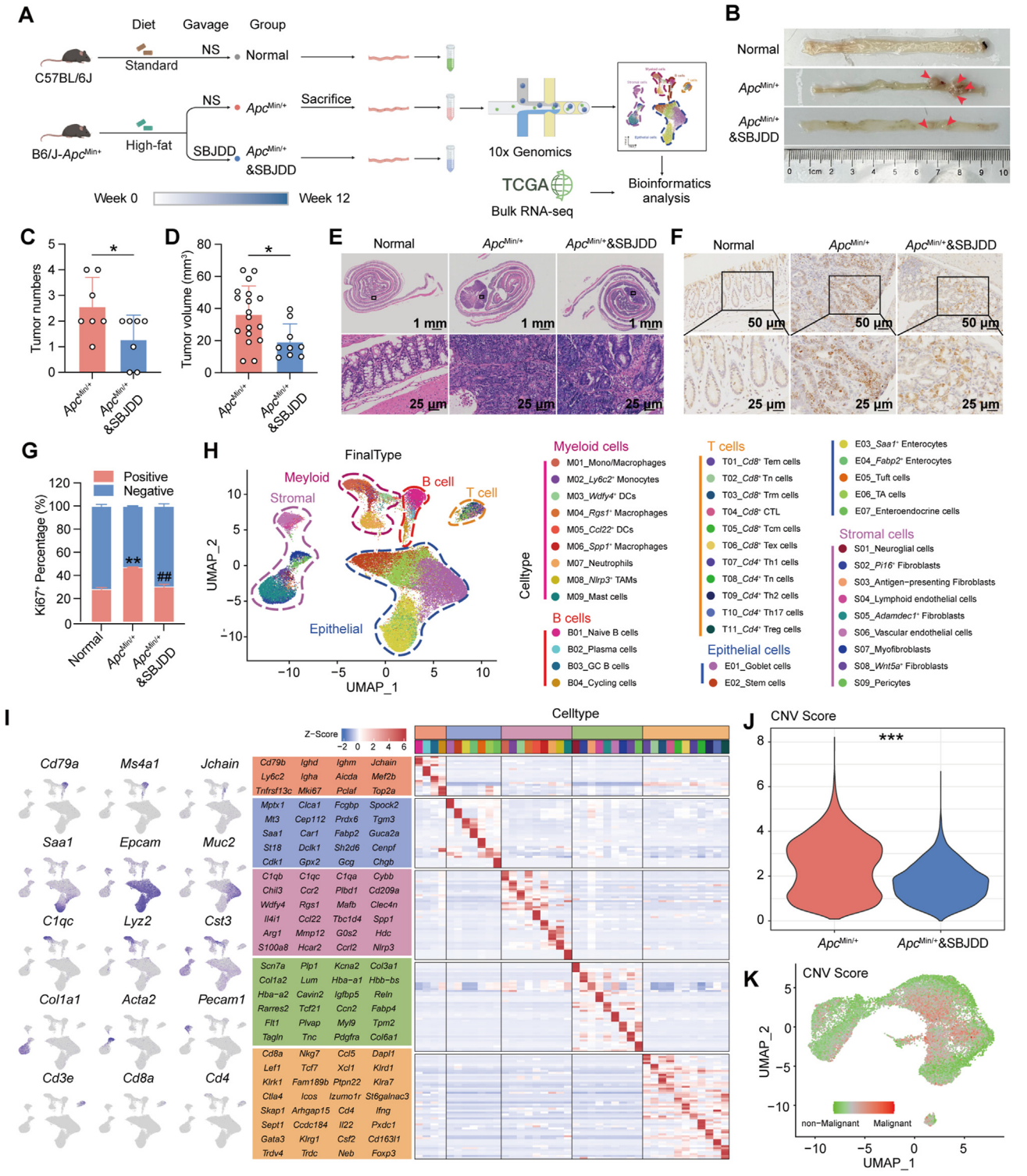

Figure 1 The effect of Shen-Bai-Jie-Du decoction (SBJDD) on tumorigenesis and copy number variation (CNV) patterns in *Apc*$^{Min/+}$ mice. (A) Schematic diagram of the experimental workflow. (B−D) Comparison of tumor number and volume among groups. Red arrowheads indicate colorectal tumors. (E) Hematoxylin and eosin staining of the colorectum among groups. (F, G) Immunohistochemistry (IHC) analysis of Ki67-positive cells in colorectal tumor tissues. (H) UMAP plot displaying the clustering of 48,992 single cells. (I) Forty distinct cell subtypes were identified. Cell subtypes were annotated using known markers, and each subtype is color-coded. (J) UMAP plot of malignancy levels in epithelial cell subgroups. (K) Violin plot shows CNV scores of epithelial cells. Data are presented as mean ± SD ($n = 7$). *$P < 0.05$, **$P < 0.01$, ***$P < 0.001$ compared to the normal group; $^{\#\#}P < 0.01$ compared to the *Apc*$^{Min/+}$ group.

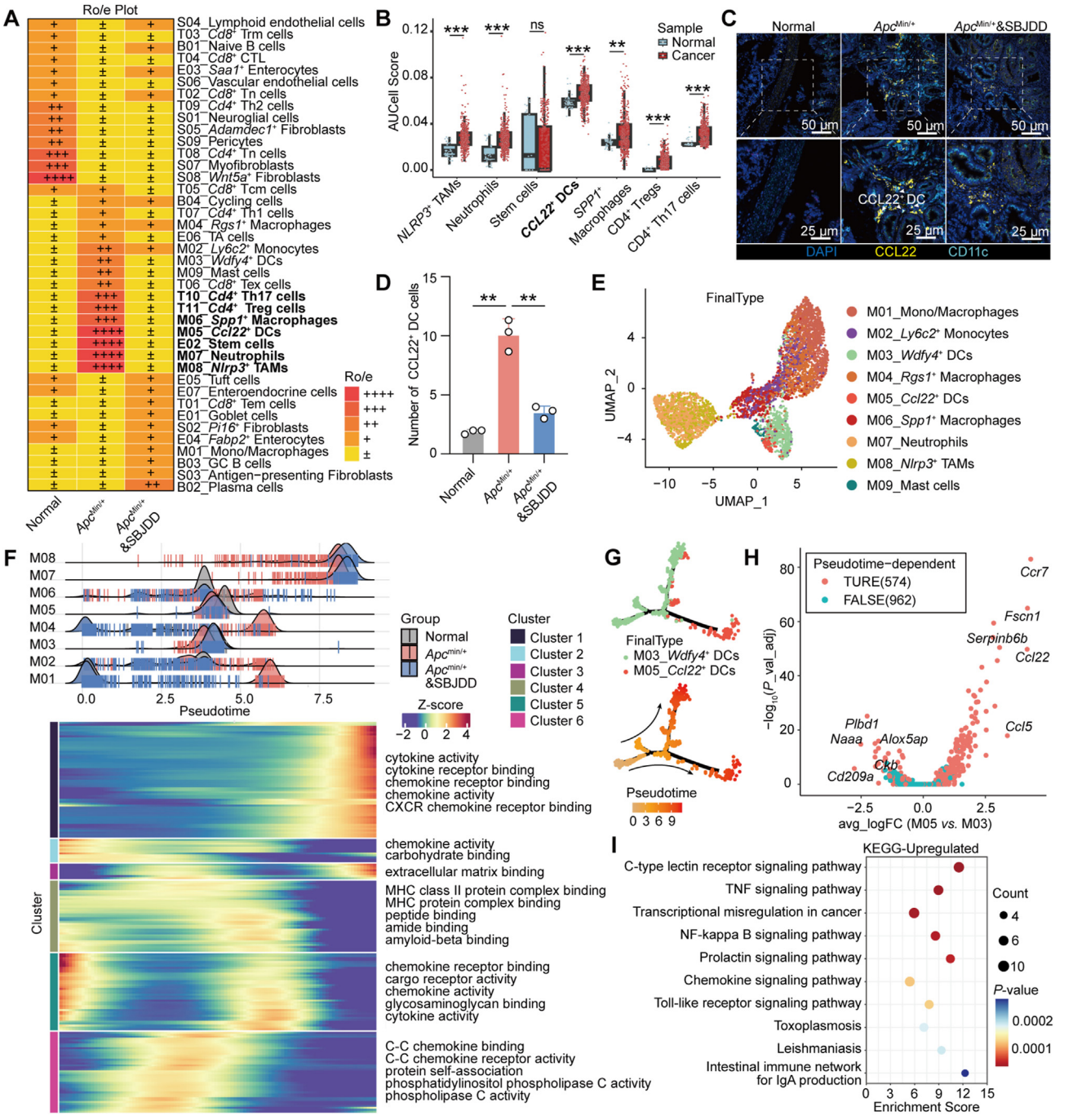

Figure 2 Dynamic alterations and the development trajectory of *Ccl22*$^+$ dendritic cells (DCs) in tumor microenvironment. (A) Heatmap of the observed to expected cell numbers (Ro/e) ratio for each cell cluster. ±, 0≤Ro/e < 1; +, 1≤Ro/e < 1.5; ++, 1.5≤Ro/e < 2; +++, 2≤Ro/e < 2.5; ++++, Ro/e ≥ 2.5; (B) AUCell scores of each cell subgroup in normal and colorectal cancer (CRC) groups based on the cancer genome atlas (TCGA) database. (C, D) Multiplex immunohistochemistry (mIHC) shows the infiltration of CCL22$^+$ DCs in different groups. (E) UMAP plot displaying 9 myeloid cell subtypes. (F) Pseudo-time analysis mapping the dynamic evolution of myeloid cell subtypes during colorectal tumorigenesis and SBJDD treatment. (G) Pseudo-time trajectory analysis shows the developmental origin of *Ccl22*$^+$ DCs from *Wdfy4*$^+$ DCs. (H) Scatter plot of Pseudo time-dependent genes in *Ccl22*$^+$ DCs. (I) Kyoto Encyclopedia of Genes and Genomes (KEGG) pathway analysis of pseudo-time-dependent upregulated genes in *Ccl22*$^+$ DCs. Data are presented as mean ± SD ($n = 3$). ns, no significance; $^{**}P < 0.01$, $^{***}P < 0.001$.

assemble myeloid differentiation trajectories, except for mast cells. We found that M01 was in a relatively initial differentiation position, M03 and M05 were located in the lower part of the differentiation trajectory, and M05 was more terminal than M03. In addition, M07 and M08 have similar differentiation status, which are located at the end of differentiation and are enriched in *Apc*$^{Min/+}$ and *Apc*$^{Min/+}$ & SBJDD, suggesting that these 2 cell populations may have similar roles in the development of

adenomas (Fig. S3B). Subsequently, we identified genes that showed significant changes during differentiation and grouped them into 6 clusters *via* hierarchical clustering. Among them, the genes in Cluster 4 were highly expressed in the pseudo-time interval enriched in M03 and M05. GO analysis showed that GO terms such as MHC II complex binding and peptide binding were significantly enriched in the Cluster 4 gene, which was closely related to the antigen presentation function of *Apc* cells (Fig. 2F).

Subsequent studies of DC development trajectory confirmed that *Ccl22*$^+$ DCs were derived from *Wdfy4*$^+$ DCs (Fig. 2G). We screened for pseudo-time-dependent genes to clarify the functional changes during *Ccl22*$^+$ DCs development (Fig. 2H). GO analysis of these genes indicated that upregulated genes were enriched in functions like kinase activator activity, kinase regulator activity, and cytokine receptor binding. In contrast, downregulated genes were mainly related to MHC class II protein complex binding, MHC protein complex binding, and immune receptor activity (Fig. S3C). By Kyoto Encyclopedia of Genes and Genomes (KEGG) analysis, upregulated genes were enriched in the C-type lectin receptor signaling pathway, TNF signaling pathway, and transcriptional mis-regulation in cancer; downregulated genes mainly participated in such pathways as antigen processing and presentation, ribosome and thyroid hormone synthesis pathways (Fig. 2I, Fig. S3D).

3.6. *The potential immunosuppressive action of CCL22*$^+$ *DCs*

To further explore the role of CCL22$^+$ DCs in the TME, we analyzed the interaction intensity between DCs and various T cell types. The results showed that compared to the normal group, the *Apc*$^{Min/+}$ group exhibited significantly enhanced communication between DCs and *Cd8*$^+$ Tem cells, *Cd8*$^+$ Tn cells, *Cd8*$^+$ Trm cells, *Cd8*$^+$ CTL cells, and *Cd4*$^+$ Tregs. SBJDD effectively reversed these effects (Fig. 3A). Next, we examined the communication intensity and associated molecules between different DC subsets. The results revealed that *Ccl22*$^+$ DCs have significantly stronger interactions with *Cd4*$^+$ Tregs than *Wdfy4*$^+$ DCs, primarily mediated by *Cd80*/*Cd86* and *Ctla4* (Fig. 3B). Violin plots demonstrated significant expression of *Cd80* and *Cd86* in M05 *Ccl22*$^+$ DCs and *Ctla4* in T11 *Cd4*$^+$ Tregs (Fig. S3E). mIHC staining confirmed the presence of CCL22$^+$ DCs and demonstrated changes in the abundance of CCL22$^+$ DCs and CD4$^+$ FOXP3$^+$ Tregs across different groups. Moreover, the average distance between CCL22$^+$ DCs and CD4$^+$ FOXP3$^+$ Tregs was significantly reduced in the *Apc*$^{Min/+}$ group, and SBJDD treatment increased this distance (Fig. 3C).

Based on scRNA-seq data, we performed a deconvolution analysis using the TCGA database. We found that the abundance of *CCL22*$^+$ DCs was significantly higher in CRC tissues than in normal intestinal tissues, particularly in microsatellite-stable CRC (Fig. 3D). Additionally, we selected some representative functional genes of Tregs and marker genes of *CCL22*$^+$ DCs for correlation analysis. The expression of *CCL22* was significantly correlated with those of *FOXP3* and *CTLA4* in the TCGA database (Fig. 3E). Furthermore, we examined the abundance of CCL22$^+$ DCs and CD4$^+$ FOXP3$^+$ Tregs in TMA, which results showed a significant increase in the abundance of CCL22$^+$ DCs and CD4$^+$ FOXP3$^+$ Tregs in CRC tissues (Fig. 3F, Fig. S3F and S3G). The clinical characteristics of the TMA patients are listed in Supporting Information Table S4. Correlation analysis revealed a significant positive correlation between the abundance of CCL22$^+$ DCs and CD4$^+$ FOXP3$^+$ Tregs in the TMA ($R = 0.647$, Fig. 3G). In addition, the abundance of CCL22$^+$ DCs and CD4$^+$ FOXP3$^+$ Tregs was significantly higher in the tissues of CRC patients younger than 60 years old, with no significant correlation found with tumor location, grade, or stage (Supporting Information Table S5).

3.7. *Similar mechanisms of microenvironment after SBJDD treatment in the clinic*

Based on the results of the above experiments and previous clinical trials[13], we collected clinical paired samples for scRNA-seq to further clarify the mechanism of SBJDD in preventing colorectal tumorigenesis (Fig. 4A). Colonoscopy revealed that SBJDD treatment reduced the volume of colorectal adenoma (Fig. 4B). A total of 39,500 cells were generated for the identification of cell subtypes. Seventeen cell subtypes were defined, including T cells, Tregs, and memory T cells (Fig. 4C). The marker genes of these cells are listed in Supporting Information Fig. S4A. Subsequently, we performed CNV analysis on epithelial cells and found that the CNV scores in adenoma tissues were significantly reduced after SBJDD treatment (Fig. 4D). SBJDD altered the ratio of various cell subtypes in the tumor microenvironment, significantly reducing DCs and Tregs (Fig. 4E, Fig. S4B). Furthermore, DCs were divided into 2 subtypes, DC_1 and DC_2, significantly reduced after SBJDD treatment. Pseudo-time analysis revealed that DC_2 is at the end of the developmental trajectory, originating from DC_1, and is accompanied by the downregulation of MHC genes (Fig. 4F, Fig. S4C). A comparison of molecular expression between DC_1/2 and M03/M05 DCs showed that DC_1 cells share similar molecular characteristics with M03 DCs, while DC_2 cells resemble M05 *Ccl22*$^+$ DCs (Fig. 4G).

3.8. *LPS combined with cholesterol-induced CCL22*$^+$ *DCs in vitro*

Based on previous studies[26], we isolated immature DCs (imDCs) and induced their maturation (Supporting Information Fig. S5A and S5B). Given the significant role of a high-fat diet in developing colorectal tumors, we measured the total cholesterol levels in mouse serum. The results showed that mice fed with a high-fat diet had significantly elevated total cholesterol levels (Fig. 5A). However, imDCs treated with cholesterol did not significantly regulate the expression of *Cd80*, *Cd83*, *Cd86*, and *Ccl22* (Fig. S5C). CD83, an important marker of DC maturation, is significantly increased in M05 *Ccl22*$^+$ DCs (Fig. 5B). We then treated imDCs with both LPS and cholesterol. Compared to single treatments, the combination significantly promoted the expression of characteristic *Ccl22*$^+$ DC genes, including *Cd80*, *Cd83*, *Cd86*, *Ccl22*, and *Ccr7* (Fig. 5C, Fig. S5D). Flow cytometry showed a significant increase in the mean fluorescence intensity (MFI) value of CCR7 in DCs after combined treatment with LPS and cholesterol (Fig. S5E). Additionally, we isolated naïve CD4$^+$ T cells using magnetic bead sorting and induced them into Tregs as previously reported[27] (Fig. S5F and S5G). Subsequently, we co-cultured induced *Ccl22*$^+$ DCs with Tregs and measured the levels of CTLA4 in Tregs. The results showed that LPS-stimulated DCs significantly reduced the MFI value of CTLA4 in Tregs, while the induced *Ccl22*$^+$ DCs restored the MFI value of CTLA4 (Fig. 5D, Fig. S5H).

3.9. *SBJDD inhibited colorectal tumorigenesis via CCL22*$^+$ *DCs*

To investigate whether SBJDD inhibits colorectal tumorigenesis *via* CCL22$^+$ DCs, we administered induced *Ccl22*$^+$ DCs

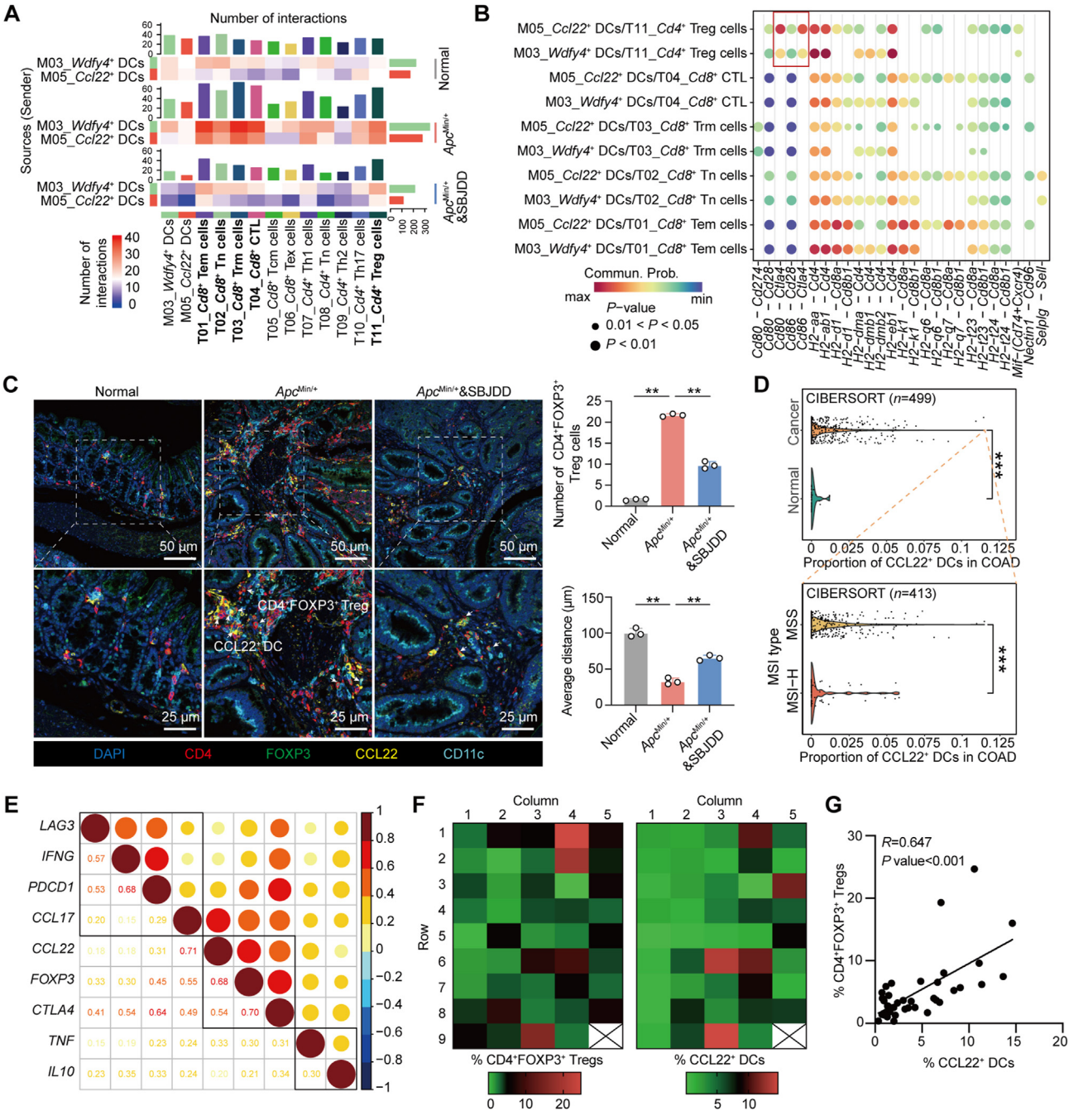

Figure 3 The potential immunosuppressive action of CCL22^{+} DCs. (A) The interaction intensity between DCs and various T cell types in different groups. (B) Communication intensity and associated molecules between different DC subsets and *Cd4*$^{+}$ regulatory T cells (Tregs). (C) mIHC shows the abundance and spatial distance changes of CCL22^{+} DCs and Tregs in different groups. (D) Deconvolution analysis based on the TCGA database shows the abundance of *CCL22*$^{+}$ DCs in CRC and normal tissues. (E) Correlation analysis shows a significant association between the expression of characteristic genes of *CCL22*$^{+}$ DCs and Tregs. (F) The positive rates of CD4^{+} FOXP3^{+} Tregs or CCL22^{+} DCs in a tissue microarray (TMA). The locations of column 1 (rows 1 to 9), column 2 (rows 1 to 6), and column (row 5) in the TMA are colorectal adenoma tissues, and the others are cancer tissues. Detailed characteristics of the TMA patients are provided in Table S1. (G) Correlation between the positive rates of CD4^{+} FOXP3^{+} Tregs and CCL22^{+} DCs in TMA. Data are presented as mean ± SD ($n = 3$). $^{**}P < 0.01$, $^{***}P < 0.001$.

intraperitoneally to *Apc*$^{Min/+}$ mice. The mice were divided into 4 groups based on different interventions: *Apc*$^{Min/+}$ group, SBJDD group, *Ccl22*$^{+}$ DC group, and *Ccl22*$^{+}$ DC combined with the SBJDD treatment group. Our findings indicated that SBJDD significantly reduced the number and size of tumors in *Apc*$^{Min/+}$ mice, whereas the intraperitoneal injection of *Ccl22*$^{+}$ DCs attenuated the therapeutic effect of SBJDD (Fig. 5E and F). The groups had no statistically significant differences in the body weight curves (Fig. 5G). Hematoxylin and eosin staining revealed that the injection of *Ccl22*$^{+}$ DCs mitigated the improvement in the pathological grading of colorectal tumors by SBJDD (Fig. 5H). Furthermore, IHC results showed that SBJDD reduced the

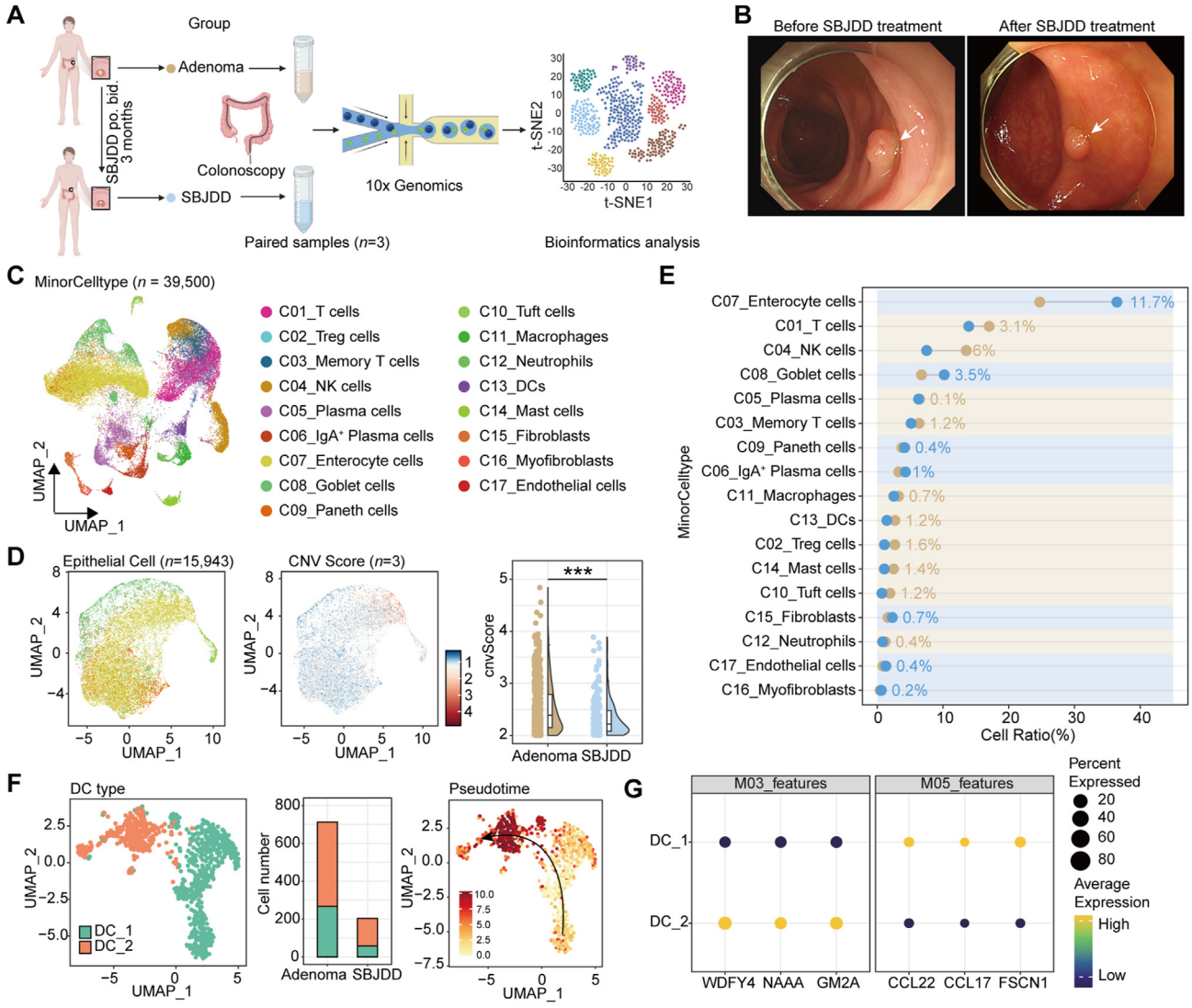

Figure 4 Single-cell transcriptomic analysis in clinical paired samples. (A) Schematic diagram of single-cell RNA sequencing experiment on paired samples from patients with multiple colorectal adenomas. (B) Colonoscopy shows morphological changes of the same adenoma before and after SBJDD treatment. (C) UMAP plot displaying the clustering of 39,500 single cells in colorectal adenoma samples before and after SBJDD treatment. (D) CNV scores of epithelial cells before and after SBJDD treatment ($n = 3$). (E) Changes in cell ratio of each subtype before and after SBJDD treatment. (F) DC subtypes and development trajectory. (G) Similarity of DC subtypes in the two scRNA-seq results. ***$P < 0.001$.

proportion of Ki67-positive cells in the tissues, an effect reversed by injecting *Ccl22*$^{+}$ DCs (Fig. 5I).

To determine whether the cellular composition of the microenvironment was altered across different groups, we performed mIHC to assess the infiltration of CCL22^{+} DCs and Tregs in the tissues. The results demonstrated that, compared to the *Apc*$^{Min/+}$ group, the SBJDD group exhibited significantly lower proportions of CCL22^{+} DCs and Tregs, whereas no significant differences were observed in the CCL22^{+} DC group. Compared to the SBJDD group, the intraperitoneal injection of CCL22^{+} DCs significantly increased the infiltration of CCL22^{+} DCs and Tregs in the tissues (Fig. 5J and K). Additionally, we measured the levels of total cholesterol and CCL22 in the serum of mice, finding no statistically significant differences among the groups (Fig. 5L, Fig. S5I). SBJDD significantly reduced the *Ccl22* and *Ccr7* mRNA expression in tissues, whose effect was reversed by *Ccl22*$^{+}$ DCs (Fig. 5M).

3.10. TMEM131 derived CCL22^{+} *DCs generation by TNF signaling pathway*

We performed gene expression profiling analysis in each group to elucidate the mechanism by which SBJDD could regulate the differentiation of CCL22^{+} DCs. DEGs including *Epb41*, *Cxcl9*, and *Tmem131* were identified (Fig. 6A). A Venn diagram was drawn based on the DEGs of the above genes and pseudo-time-dependent expressed genes, showing an intersection gene as *Tmem131* (Fig. 6B). *Tmem131* was upregulated during *Ccl22*$^{+}$ DC differentiation according to the scRNA-seq data (Fig. 6C). qPCR results demonstrated that the *Tmem131* was upregulated in the tissues of the *Apc*$^{Min/+}$ group, and downregulated after SBJDD treatment (Fig. 6D, Supporting Information Fig. S6A). *Tmem131* mRNA expression was also elevated in *Ccl22*$^{+}$ DCs (Fig. 6E). Subsequently, we knocked down TMEM131 expression in *Ccl22*$^{+}$ DCs and found that TMEM131 knockdown downregulated the

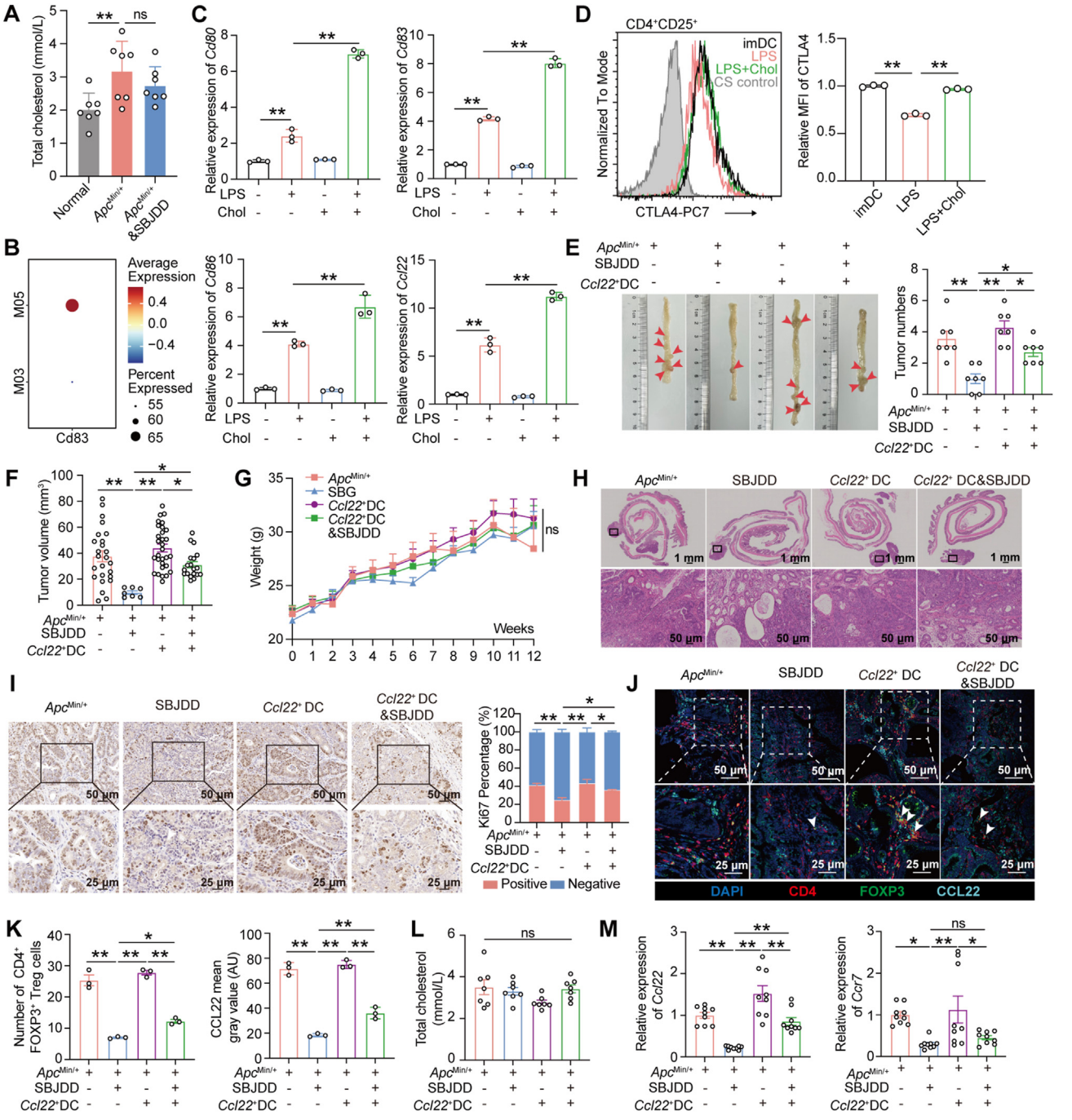

Figure 5 SBJDD inhibited colorectal tumorigenesis *via* CCL22^{+} DCs. (A) Measurement of total cholesterol levels in mouse serum (B) Differential expression of CD83 in M05 *Ccl22*$^{+}$ DCs and M03 *Wdfy4*$^{+}$ DCs. (C) Gene expression analysis of imDCs treated with lipopolysaccharide, cholesterol, and their combination. (D) Flow cytometry analysis of the mean fluorescence intensity (MFI) value of CTLA4 in CD4^{+}CD25^{+} Tregs after co-culture with different DCs. (E, F) Comparison of tumor number and volume among groups of *Apc*$^{Min/+}$ mice. Red arrowheads indicate colorectal tumors. (G) Changes in body weight of *Apc*$^{Min/+}$ mice in different groups. (H) Hematoxylin and eosin staining of colorectal tumor tissues. (I) IHC analysis of Ki67-positive cells in colorectal tumor tissues. (J, K) mIHC analysis shows the infiltration of CCL22^{+} DCs and Tregs in the colorectal tumor tissues. (L) Measurement of total cholesterol levels in mouse serum. (M) qPCR analysis of *Ccl22* and *Ccr7* in colorectal tumor tissues. Data are presented as mean ± SD ($n = 7$). ns, no significance; *$P < 0.05$, **$P < 0.01$.

mRNA expression of *Ccl22*, *Cd80*, and *Cd86*, but not *Cd83* (Fig. 6F, Fig. S6B). mRNA sequencing was performed to detect the DEGs after TMEM131 knockdown (Fig. 6G). KEGG analysis revealed that upregulated genes were enriched in such pathways as cell cycle, pyrimidine metabolism, and one-carbon pool by folate; downregulated genes were enriched in such pathways as TNF signaling pathway, cytokine−cytokine receptor interaction, and Epstein−Barr virus infection (Fig. 6H). TMEM131 and TNF signaling pathway were significantly enriched in CCL22^{+} DCs (Fig. 6I). TMEM131 was also significantly correlated with TNF in

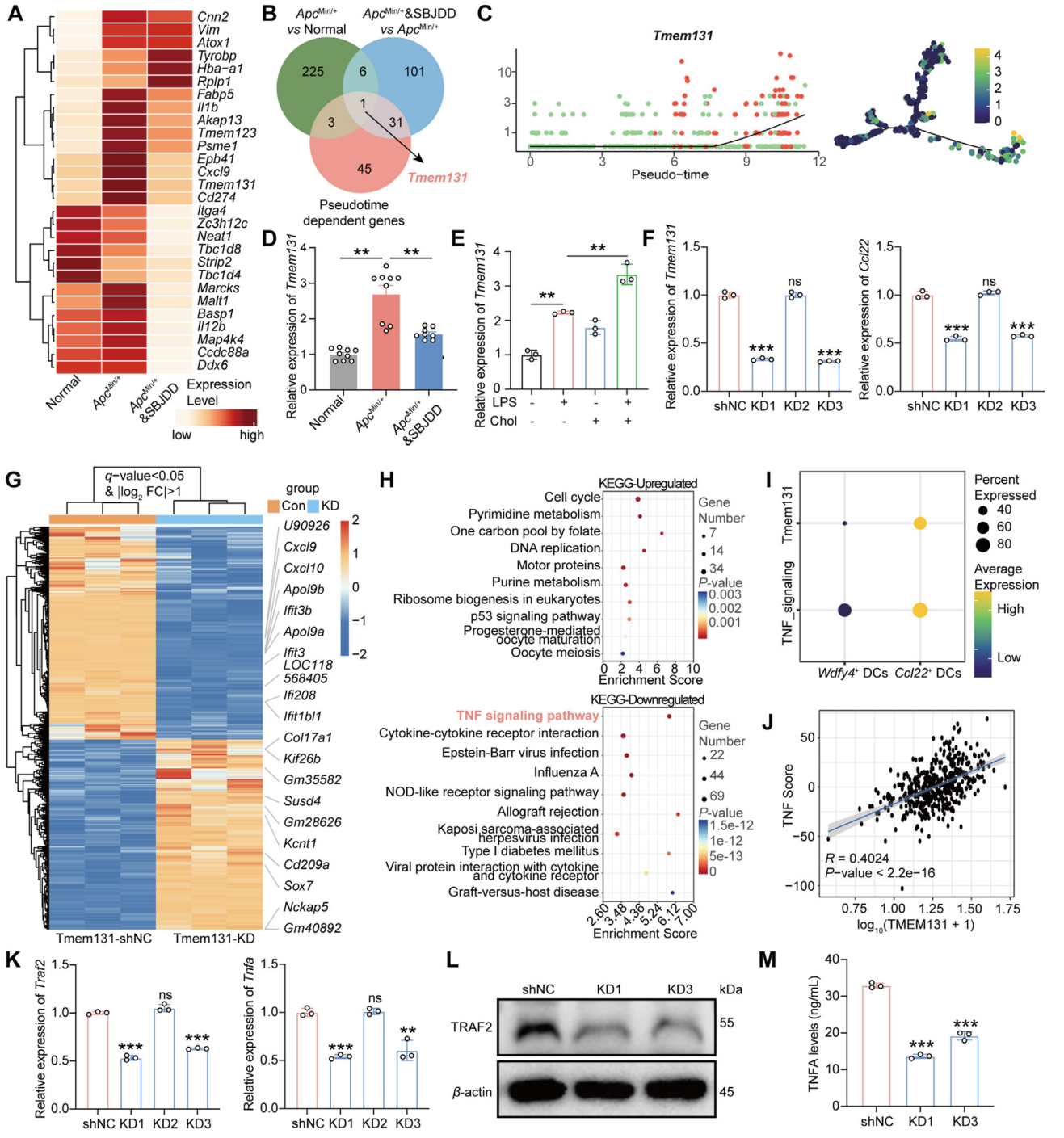

Figure 6 TMEM131 regulates CCL22$^+$ DCs generation by the TNF signaling pathway. (A) The heatmap shows the differentially expressed genes (DEGs) in *Ccl22*$^+$ DCs from different groups. (B) Venn diagram identifies intersecting genes between DEGs in different groups and pseudo-time-dependent genes. (C) Dynamic changes in *Tmem131* expression during the differentiation of *Ccl22*$^+$ DCs from *Wdfy4*$^+$ DCs. (D, E) qPCR analysis of *Tmem131* mRNA expression in colorectal tissue samples and *Ccl22*$^+$ DCs. (F) qPCR analysis of *Tmem131* and *Ccl22* mRNA expression after TMEM131 knockdown. (G) DEGs after TMEM131 knockdown. (H) KEGG pathway analysis of upregulated/downregulated genes after TMEM131 knockdown. (I) The enrichment of Tmem131 and TNF signaling pathway in DC subtypes. (J) The correlation between TMEM131 and TNF pathway in TCGA datasets ($n = 499$). (K) qPCR analysis of *Traf2* and *Tnfa* mRNA expression after TMEM131 knockdown. (L) Western blot analysis of TRAF2 protein levels after TMEM131 knockdown. (M) ELISA analysis of TNFA protein levels after TMEM131 knockdown. Data are presented as mean ± SD ($n = 3$). ns, no significance; $^{**}P < 0.01$, $^{***}P < 0.001$.

TCGA datasets (Fig. 6J). Western blot, ELISA, and qPCR demonstrated that TMEM131 positively regulated the expression of TRAF2 and TNFA (Fig. 6K−M).

3.11. SBJDD and its active compound berberine modulate the function of CCL22$^+$ DCs via binding with TMEM131

A previous study has identified the chemical components of SBJDD[13]. Ultrahigh-performance liquid chromatography with quadrupole time-of-flight mass spectrometry was performed to further explore the active components of SBJDD *in vivo*. The positive and negative ion modes of the chemical base peak ion chromatogram (BPI) of SBJDD serum were used to classify them into 2 categories (Fig. 7A and B). Supporting Information Table S6 lists and describes the prototype compounds found in plasma. There were 28 prototype compounds, including 7 alkaloids, 6 flavonoids, 5 amino acids, 4 miscellaneous, 2 terpenoids, 1 anthraquinone, 1 phenylpropanoid, 1 phenol, and 1 other (Fig. 7C). The source of these compounds is summarized in Fig. 7D. We also examined the distribution of representative components in tissues and found that berberine accumulated significantly in intestinal tissues (Fig. 7E). So, we performed quantitative analysis of berberine using ultrahigh-performance liquid chromatography with triple-quadrupole linear ion-trap tandem mass spectrometry (UHPLC−QTRAP−MS/MS) system and confirmed a significant increase in berberine content in SBJDD-containing serum (Fig. S6C and S6D). Molecular docking between berberine and TMEM131 protein was carried out using CB-Dock2 software, and the docking score was −7.5 kcal/mol (Fig. 7F and G). We prepared SBJDD-containing serum and treated the induced Ccl22$^+$ DCs with different concentrations to evaluate the impact of SBJDD. SBJDD and berberine significantly reduced the expression of *Ccl22* and *Ccr7* (Fig. 7H, Fig. S6E and S6F), as well as the MFI value of CCR7 in induced *Ccl22*$^+$ DCs (Fig. S6G and S6H). Co-culture experiments demonstrated that SBJDD- or berberine-treated induced *Ccl22*$^+$ DCs reduced CTLA4 expression in Tregs (Fig. 7I, Fig. S6I). Berberine also inhibited the mRNA and protein levels of TRAF2 and TNFA in CCL22$^+$ DCs (Fig. 7J and K, Fig. S6J). Surface plasmon resonance analysis was conducted to confirm the affinity between TMEM131 and berberine using the recombinant protein, and the K_D value was 5.03×10^{-6} mol/L (Fig. 7L).

4. Discussion

Accumulating evidence suggests that TME is closely involved in the initiation and progression of tumors[28]. Single-cell sequencing technology has been extensively applied in TME-related studies. A study on the dynamic alteration of epithelial cells in TME revealed that developmental reprogramming mediated plasticity of abnormal cell states is an early critical event in colorectal tumorigenesis[29]. Another scRNA-seq study in familial adenomatous polyposis patients demonstrated increasing immunosuppression in the TME during early CRC progression[30]. Heiser et al.[6] further reported that at the onset of sporadic CRC, an immunosuppressive microenvironment forms, characterized by reduced T-cell infiltration, increased immunosuppressive myeloid cells, and activated DCs.

TCM plays a crucial role in CRC prevention and treatment. Previous studies have demonstrated that TME can be regulated by Chinese medicine[12]. Despite the complexity of TCM components and their interactions within TME, further molecular mechanism exploration is feasible through UHPLC−QTRAP−MS/MS and single-cell sequencing. Our previous studies have demonstrated a dose-dependent effect and the clinical safety of SBJDD against CRC[13,31]. This study focuses on the TME landscape during colorectal tumorigenesis and SBJDD treatment. We confirmed that SBJDD significantly inhibits colorectal tumorigenesis in *Apc*$^{Min/+}$ mice and clinical patients (Figs. 1B−D, 4B). scRNA-seq depicted the TME landscape and suggested a higher CNV score in the *Apc*$^{Min/+}$ group (Figs. 1H−J, 4D). These results demonstrated that SBJDD effectively retarded colorectal tumorigenesis.

Besides, we discovered a notable increase in *Ccl22*$^+$ DCs, neutrophils, and *Nlrp3*$^+$ TAMs in colorectal tumors from *Apc*$^{Min/+}$ mice (Fig. 2A). The oncogenic role of CCL22$^+$ DCs in CRC is also supported by AUCell scores from the TCGA database (Fig. 2B). mIHC and qPCR analyses confirmed dynamic changes in CCL22$^+$ DCs under different conditions (Fig. 2C, Fig. S2E), aligning with previous findings on DC activation in early CRC stages[6]. However, previous studies did not explore the function of abnormal DC activation. Our analysis revealed that *Ccl22*$^+$ DCs derive from *Wdfy4*$^+$ DCs and exhibit enhanced interactions with Tregs (Figs. 2G, 3A−C). Pseudo-time analysis indicates that the differentiation process and gene change from DC_1 to DC_2 are similar to those in mice (Fig. 4F, Fig. S4C). Existing data have clarified that CCL22 is a crucial chemokine for Tregs, which leads to their migration[32]. Our study identified that SBJDD reduces *Ccl22*$^+$ DCs and Tregs infiltration in the TME (Figs. 2A−C, 4E, Fig. S4B). Remarkably, SBJDD only reduced *Ccl22* and *Ccl17* mRNA expression but did not affect the plasma levels of CCL22 and CCL17 (Fig. S2E and S2F). The complexity of the source of plasma components may mask the effective regulation of SBJDD in the microenvironment. Besides, *Cd80/86* and *Ctla4* are primary molecules facilitating *Ccl22*$^+$ DCs and Tregs interaction (Fig. 3B and C, Fig. S3E). Correlation analysis reveals a significant link between the abundance of CCL22$^+$ DCs and CD4$^+$ FOXP3$^+$ Tregs in colorectal tissues ($R = 0.647$, Fig. 3F and G). Taken together, CCL22$^+$ DCs may exert an immunosuppressive effect by directly recruiting Tregs or regulating the function of Tregs *via* CTLA4 molecules.

High-fat diets are well-established risk factors for CRC and cholesterol homeostasis enhances colorectal tumor formation[33,34]. Overweight or obese CRC patients experience attenuated antigen-presenting functions of DCs, notably in MHC class II molecules, limiting T-cell activation and aggravating the formation of an immunosuppressive microenvironment[35]. We noticed total cholesterol levels increased in *Apc*$^{Min/+}$ mice (Fig. 5A). To further clarify the role of *Ccl22*$^+$ DCs on tumorigenesis, we induced the *Ccl22*$^+$ DCs *in vitro* using LPS and cholesterol and demonstrated the function and expression of markers (Fig. 5B−D, Fig. S5C−S5H). It is well known that LPS induces the activation of DCs, and this activation does not exhaust DCs[36,37]. CCL22$^+$ DCs had some molecular characteristics of mature DCs, but their antigen presentation ability was significantly down-regulated. Based on these findings, we suggest that CCL22$^+$ DCs may represent an "exhausted" type of DC and that adding cholesterol during DC maturation promotes their differentiation into "exhausted DCs". Moreover, the infusion of *Ccl22*$^+$ DCs into mice *via* intraperitoneal injection did not significantly increase the number of colorectal tumors in *Apc*$^{Min/+}$ mice; however, it markedly diminished the therapeutic efficacy of SBJDD (Fig. 5E−I). One possible reason is that the control *Apc*$^{Min/+}$

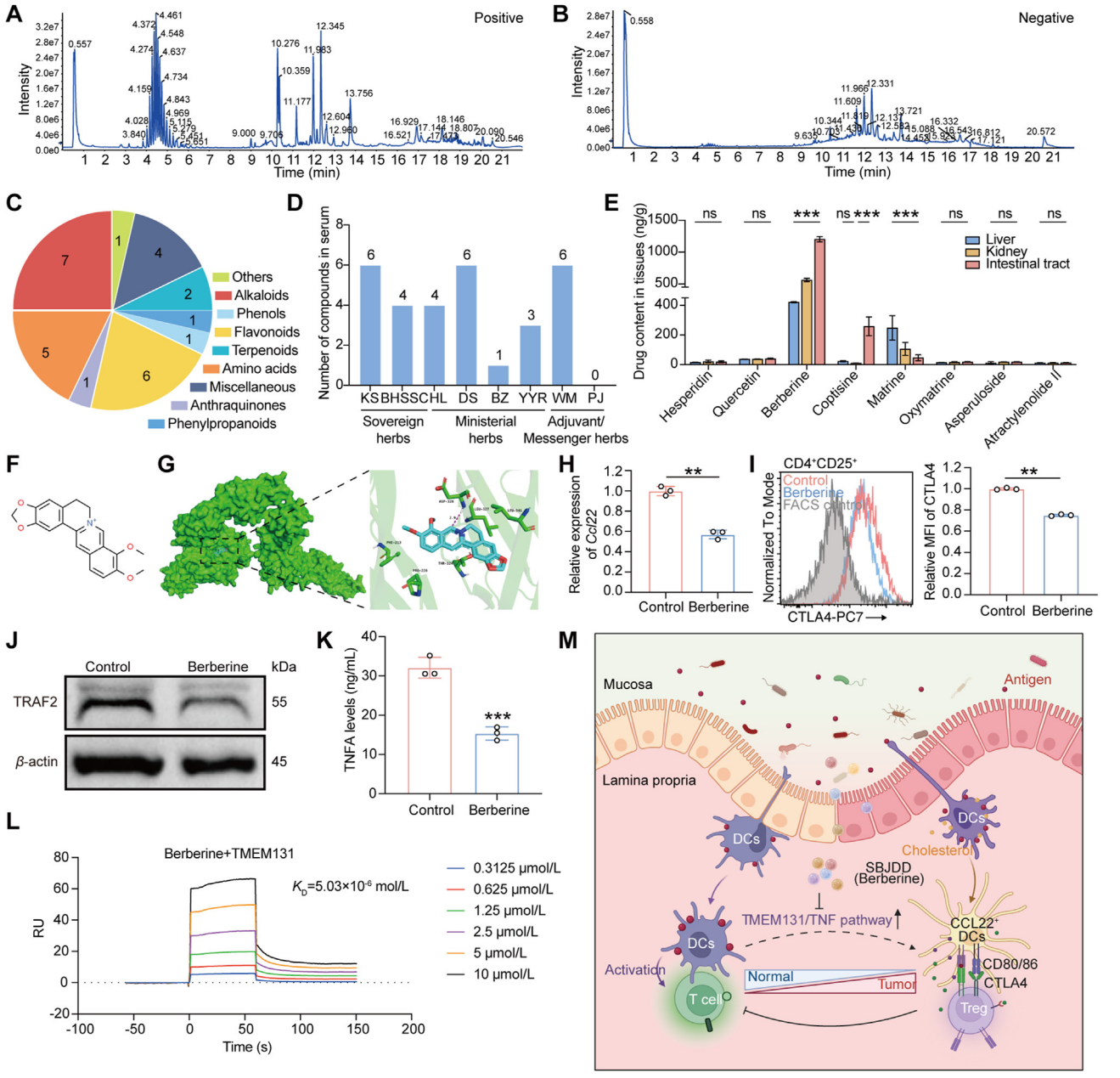

Figure 7 SBJDD and its active compound berberine modulated the function of CCL22$^+$ DCs *via* binding with TMEM131. The chemical base peak ion (BPI) chromatogram of SBJDD plasma in the positive (A) and negative (B) ion mode using ultrahigh-performance liquid chromatography with quadrupole time-of-flight mass spectrometry. (C) Structural classification of prototype compounds in plasma. (D) The number of prototype compounds in plasma for each herb. (E) Tissue distribution of typical compounds of SBJDD. (F) The chemical structure of berberine. (G) Molecular docking results for TMEM131 (AlphaFold ID: AF-O70472-F1) with berberine. (H) Gene expression analysis of CCL22$^+$ DCs treated with berberine (20 μmol/L). (I) The MFI value of CTLA4 in CD4$^+$CD25$^+$ Tregs after co-culture with *Ccl22*$^+$ DCs treated with berberine. (J, K) The protein levels of TRAF2 and TNFA in *Ccl22*$^+$ DCs after berberine treatment. (L) Surface plasmon resonance assay obtained separately on TMEM131-coated chip in the presence of different concentrations of berberine. (M) Diagram of the mechanism of SBJDD retards colorectal tumorigenesis. Data are presented as mean ± SD ($n = 3$). ns, no significance; $^{**}P < 0.01$, $^{***}P < 0.001$.

mice were also on a high-fat diet, which had already resulted in a significant presence of *Ccl22*$^+$ DCs in their microenvironment. In SBJDD-treated mice, the injection of *Ccl22*$^+$ DCs increased the number and volume of tumors. These results confirm that SBJDD inhibits colorectal tumorigenesis by reducing the infiltration of CCL22$^+$ DCs with immunosuppressive action.

Furthermore, *Tmem131* was screened for differentially expressed genes during *Ccl22*$^+$ DCs differentiation and SBJDD treatment (Fig. 6A–C). qPCR demonstrated its mRNA expression levels in tissues and induced *Ccl22*$^+$ DCs (Fig. 6D and E, Fig. S6A). TMEM131 is a transmembrane protein that regulates endoplasmic reticulum stress and collagen production[38]. A

previous study has reported that TMEM131 is a potential therapeutic target of CRC[39]. Subsequently, we knocked down TMEM131 and found that TMEM131 positively regulated the expression of *Ccl22*$^+$ DCs-related marker genes (Fig. 6F, Fig. S6B). However, TMEM131 knockdown did not affect the expression of *Cd83* (Fig. S6B). Bulk-RNAseq also demonstrated this regulatory relationship, and KEGG analysis suggested related pathways (Fig. 6H). It was remarkable that the TNF signaling pathway was also associated with the differentiation trajectory of *Ccl22*$^+$ DCs (Fig. 6I). We also demonstrated the regulatory effect of TMEM131 on the TNF signaling pathway in *Ccl22*$^+$ DCs (Fig. 6K−M). These results indicated that TMEM131 may regulate the differentiation of CCL22$^+$ DCs *via* the TNF signaling pathway.

Finally, we explored potential effective constituents in SBJDD using ultrahigh-performance liquid chromatography with quadrupole time-of-flight mass spectrometry (Fig. 7A−D). Our results found that berberine was significantly accumulated in intestinal tissues (Fig. 7E). Analysis of UHPLC−QTRAP−MS/MS further validated the presence of berberine in the serum of SBJDD-treated mice (Fig. S6C and S6D). A randomized controlled trial confirmed that berberine, a key component of SBJDD, effectively decreased the risk of colorectal adenoma recurrence[40]. Molecular docking demonstrated a strong binding affinity between TMEM131 and berberine (Fig. 7G), which was confirmed by Surface plasmon resonance assay (Fig. 7L). Besides, both SBJDD and berberine inhibited the immunosuppressive action of *Ccl22*$^+$ DCs and the expression of related marker genes (Fig. 7H, Fig. S6E−S6I). Berberine also exhibited significant inhibitory effects on the TNF signaling pathway (Fig. 7J and K, Fig. S6J). These findings suggested that SBJDD and its primary bioactive compound, berberine, suppressed colorectal tumorigenesis by regulating TMEM131-TNF signaling pathway-mediated differentiation of CCL22$^+$ DCs (Fig. 7M, created in BioRender, agreement number: VE27ZPJFIL).

5. Conclusions

This study demonstrates the significant inhibitory effects of SBJDD on colorectal tumors. scRNA-seq revealed the dynamic evolution of cell types within the TME, especially the notable accumulation of CCL22$^+$ DCs, which may represent a type of "exhausted" DC. SBJDD and its active component, berberine, interfered with colorectal tumorigenesis by reducing the immunosuppressive action of CCL22$^+$ DCs *via* the TMEM131−TNF signaling pathway. These findings suggest that harnessing the multi-component characteristics of natural products to restore the homeostasis of the TME could offer a promising new approach to treating malignant tumors.

Acknowledgments

We would like to express our sincere gratitude to Minmin Fan, Shouyu Wang, Qiuying Yan, Li Liu, and Dehua Li for their help during experiments and data analysis. We also thank Yanru Xu, Jingyang Qian, Siting Meng, and Weijuan Gao for their help with animal sampling. This work was supported by the National Key R&D Program of China (2022YFC3500200, 2022YFC3500202), National Natural Science Foundation of China (U24A20794, 82103197), Jiangsu Province Postgraduate Training Innovation Project Grant (KYCX23_2132, China), the Integrated Traditional Chinese and Western Medicine Clinical Medicine Innovation Center Fund for Colorectal Polyps from Jiangsu Province Hospital of Chinese Medicine (No.Y2023zx10) and the project funding from Jiangsu Province Hospital of Chinese Medicine (No. kgr0253, China), Natural Science Foundation of Jiangsu Province (BK20210686, China), and Nanjing University of Chinese Medicine's Key Project: "Leading the Charge with Open Competition" (AD202405, China).

Author contributions

Yuquan Tao established the ApcMin/+ mouse model and performed the gavage treatment. Yuquan Tao and Limei Gu were responsible for sample collection and submission for single-cell sequencing. Yinuo Ma analyzed single-cell sequencing data. Yuquan Tao, Limei Gu, and Ye Zhang performed validation experiments. Qinchang Zhang, Lisha Zhou, and Jie Pan assisted in the analysis of single-cell sequencing data. Meng Shen, Xuefei Zhuang, and Linmei Pan mainly conducted ultrahigh-performance liquid chromatography-related experiments. Weixing Shen and Chengtao Yu supervised and advised this project. Dan Dong and Dong Zhang assisted in the figure preparation and statistical analysis. Yuquan Tao, Yinuo Ma, and Limei Gu wrote and revised the manuscript. Yang Sun and Tingsheng Ling supervised this project and revised the manuscript. Haibo Cheng conceptualized and designed the study and approved the manuscript.

Conflicts of interest

The authors declare no competing interests.

Appendix A. Supporting information

Supporting information to this article can be found online at https://doi.org/10.1016/j.apsb.2025.05.013.

References

1. Murphy CC, Zaki TA. Changing epidemiology of colorectal cancer—birth cohort effects and emerging risk factors. *Nat Rev Gastroenterol Hepatol* 2024;**21**:25−34.
2. Nguyen LH, Goel A, Chung DC. Pathways of colorectal carcinogenesis. *Gastroenterology* 2020;**158**:291−302.
3. Fearon ER. Molecular genetics of colorectal cancer. *Annu Rev Pathol* 2011;**6**:479−507.
4. Gao M, Jiang T, Li P, Zhang J, Xu K, Ren T. Efficacy and safety of HER2-targeted inhibitors for metastatic colorectal cancer with HER2-amplified: a meta-analysis. *Pharmacol Res* 2022;**182**:106330.
5. Zhu Y, Ouyang Z, Du H, Wang M, Wang J, Sun H, et al. New opportunities and challenges of natural products research: when target identification meets single-cell multiomics. *Acta Pharm Sin B* 2022;**12**:4011−39.
6. Heiser CN, Simmons AJ, Revetta F, McKinley ET, Ramirez-Solano MA, Wang J, et al. Molecular cartography uncovers evolutionary and microenvironmental dynamics in sporadic colorectal tumors. *Cell* 2023;**186**:5620−37.e16.
7. Sathe A, Mason K, Grimes SM, Zhou Z, Lau BT, Bai X, et al. Colorectal cancer metastases in the liver establish immunosuppressive spatial networking between tumor-associated SPP1$^+$ macrophages and fibroblasts. *Clin Cancer Res* 2023;**29**:244−60.
8. Zhang L, Li Z, Skrzypczynska KM, Fang Q, Zhang W, O'Brien SA, et al. Single-cell analyses inform mechanisms of myeloid-targeted therapies in colon cancer. *Cell* 2020;**181**:442−59.e29.
9. Li J, Wu C, Hu H, Qin G, Wu X, Bai F, et al. Remodeling of the immune and stromal cell compartment by PD-1 blockade in mismatch repair-deficient colorectal cancer. *Cancer Cell* 2023;**41**:1152−69.e7.

10. Wen R, Zhou L, Peng Z, Fan H, Zhang T, Jia H, et al. Single-cell sequencing technology in colorectal cancer: a new technology to disclose the tumor heterogeneity and target precise treatment. *Front Immunol* 2023;**14**:1175343.
11. Huang MY, Chen YC, Lyu WY, He XY, Ye ZH, Huang CY, et al. Ginsenoside Rh2 augmented anti-PD-L1 immunotherapy by reinvigorating $CD8^+$ T cells *via* increasing intratumoral CXCL10. *Pharmacol Res* 2023;**198**:106988.
12. Fan X, Mai C, Zuo L, Huang J, Xie C, Jiang Z, et al. Herbal formula BaWeiBaiDuSan alleviates polymicrobial sepsis-induced liver injury *via* increasing the gut microbiota Lactobacillus johnsonii and regulating macrophage anti-inflammatory activity in mice. *Acta Pharm Sin B* 2023;**13**:1164−79.
13. Ni M, Zhang Y, Sun Z, Zhou Q, Xiao J, Zhang B, et al. Efficacy and safety of Shenbai Granules for recurrent colorectal adenoma: a multicenter randomized controlled trial. *Phytomedicine* 2024;**127**:155496.
14. Okada N, Tsujino M, Hagiwara Y, Tada A, Tamura Y, Mori K, et al. Administration route-dependent vaccine efficiency of murine dendritic cells pulsed with antigens. *Br J Cancer* 2001;**84**:1564−70.
15. Shang N, Figini M, Shangguan J, Wang B, Sun C, Pan L, et al. Dendritic cells based immunotherapy. *Am J Cancer Res* 2017;**7**:2091−102.
16. Satija R, Farrell JA, Gennert D, Schier AF, Regev A. Spatial reconstruction of single-cell gene expression data. *Nat Biotechnol* 2015;**33**:495−502.
17. Wu T, Hu E, Xu S, Chen M, Guo P, Dai Z, et al. clusterProfiler 4.0: a universal enrichment tool for interpreting omics data. *Innovation* 2021;**2**:100141.
18. Aibar S, González-Blas CB, Moerman T, Huynh-Thu VA, Imrichova H, Hulselmans G, et al. SCENIC: single-cell regulatory network inference and clustering. *Nat Methods* 2017;**14**:1083−6.
19. Qiu X, Mao Q, Tang Y, Wang L, Chawla R, Pliner HA, et al. Reversed graph embedding resolves complex single-cell trajectories. *Nat Methods* 2017;**14**:979−82.
20. Jin S, Guerrero-Juarez CF, Zhang L, Chang I, Ramos R, Kuan CH, et al. Inference and analysis of cell-cell communication using CellChat. *Nat Commun* 2021;**12**:1088.
21. Tang H, Xie H, Wang Z, Peng S, Ni W, Guo L. Economical and efficient protocol for isolating and culturing bone marrow-derived dendritic cells from mice. *J Vis Exp* 2022;**185**:e63125.
22. Fantini MC, Dominitzki S, Rizzo A, Neurath MF, Becker C. *In vitro* generation of $CD4^+$ $CD25^+$ regulatory cells from murine naive T cells. *Nat Protoc* 2007;**2**:1789−94.
23. Moreau JM, Velegraki M, Bolyard C, Rosenblum MD, Li Z. Transforming growth factor-β1 in regulatory T cell biology. *Sci Immunol* 2022;**7**:eabi4613.
24. Beyaz S, Mana MD, Roper J, Kedrin D, Saadatpour A, Hong SJ, et al. High-fat diet enhances stemness and tumorigenicity of intestinal progenitors. *Nature* 2016;**531**:53−8.
25. Zhang L, Yu X, Zheng L, Zhang Y, Li Y, Fang Q, et al. Lineage tracking reveals dynamic relationships of T cells in colorectal cancer. *Nature* 2018;**564**:268−72.
26. Liu J, Zhang X, Chen K, Cheng Y, Liu S, Xia M, et al. CCR7 chemokine receptor-inducible lnc-Dpf3 restrains dendritic cell migration by inhibiting HIF-1α-mediated glycolysis. *Immunity (Camb, Mass)* 2019;**50**:600−15.e15.
27. Xu W, Patel CH, Alt J, Zhao L, Sun IH, Oh MH, et al. GOT1 constrains TH17 cell differentiation, while promoting iTreg cell differentiation. *Nature* 2023;**614**:E1−11.
28. Jing ZQ, Luo ZQ, Chen SR, Sun ZJ. Heterogeneity of myeloid cells in common cancers: single cell insights and targeting strategies. *Int Immunopharmacol* 2024;**134**:112253.
29. Bala P, Rennhack JP, Aitymbayev D, Morris C, Moyer SM, Duronio GN, et al. Aberrant cell state plasticity mediated by developmental reprogramming precedes colorectal cancer initiation. *Sci Adv* 2023;**9**:eadf0927.
30. Hisano K, Mizuuchi Y, Ohuchida K, Kawata J, Torata N, Zhang J, et al. Microenvironmental changes in familial adenomatous polyposis during colorectal cancer carcinogenesis. *Cancer Lett* 2024;**589**:216822.
31. Huang M, Zhang Y, Ni M, Shen M, Tao Y, Shen W, et al. Shen-Bai-Jie-Du decoction suppresses the progression of colorectal adenoma to carcinoma through regulating gut microbiota and short-chain fatty acids. *Chin Med* 2024;**19**:149.
32. Bugno J, Wang L, Yu X, Cao X, Wang J, Huang X, et al. Targeting the dendritic cell-secreted immunoregulatory cytokine CCL22 alleviates radioresistance. *Clin Cancer Res* 2024;**30**:4450−63.
33. Wang B, Rong X, Palladino END, Wang J, Fogelman AM, Martin MG, et al. Phospholipid remodeling and cholesterol availability regulate intestinal stemness and tumorigenesis. *Cell Stem Cell* 2018;**22**:206−20.e4.
34. Ren Y, Wang M, Yuan H, Wang Z, Yu L. A novel insight into cancer therapy: lipid metabolism in tumor-associated macrophages. *Int Immunopharmacol* 2024;**135**:112319.
35. Xiao G, Zheng Y, Chen H, Luo M, Yang C, Ren D, et al. Single-cell transcriptome analysis reveals immunosuppressive landscape in overweight and obese colorectal cancer. *J Transl Med* 2024;**22**:134.
36. Biscari L, Kaufman CD, Farré C, Huhn V, Pacini MF, Balbi CB, et al. Immunization with lipopolysaccharide-activated dendritic cells generates a specific $CD8^+$ T cell response that confers partial protection against infection with *Trypanosoma cruzi*. *Front Cell Infect Microbiol* 2022;**12**:897133.
37. Abdi K, Singh NJ, Matzinger P. Lipopolysaccharide-activated dendritic cells: "exhausted" or alert and waiting?. *J Immunol* 2012;**188**:5981−9.
38. Zhang Z, Bai M, Barbosa GO, Chen A, Wei Y, Luo S, et al. Broadly conserved roles of TMEM131 family proteins in intracellular collagen assembly and secretory cargo trafficking. *Sci Adv* 2020;**6**:eaay7667.
39. Piran M, Sepahi N, Moattari A, Rahimi A, Ghanbariasad A. Systems biomedicine of primary and metastatic colorectal cancer reveals potential therapeutic targets. *Front Oncol* 2021;**11**:597536.
40. Chen YX, Gao QY, Zou TH, Wang BM, Liu SD, Sheng JQ, et al. Berberine *versus* placebo for the prevention of recurrence of colorectal adenoma: a multicentre, double-blinded, randomised controlled study. *Lancet Gastroenterol Hepatol* 2020;**5**:267−75.